Chinese Journal of Aeronautics, (2015),28(1): 141–151

Chinese Society of Aeronautics and Astronautics
& Beihang University

Chinese Journal of Aeronautics

cja@buaa.edu.cn
www.sciencedirect.com

Numerical simulation and transonic wind-tunnel test for elastic thin-shell structure considering fluid–structure interaction

Yan Yunju [a,*], Xi Zhuyou [a,b], Zhang Shanzhi [a]

[a] School of Mechanics, Civil Engineering and Architecture, Northwestern Polytechnical University, Xi'an 710129, China
[b] College of Science, Liaoning University of Technology, Jinzhou 121001, China

Received 17 December 2013; revised 14 August 2014; accepted 23 September 2014
Available online 26 December 2014

KEYWORDS

Aerodynamic forces;
Fluid–structure interaction;
Numerical analysis;
Thin shells;
Wind-tunnel tests

Abstract Aerodynamic force can lead to the strong structural vibration of flying aircraft at a high speed. This harmful vibration can bring damage or failure to the electronic equipment fixed in aircraft. It is necessary to predict the structural dynamic response in the design course. This paper presents a new numerical algorithm and scheme to solve the structural dynamics responses when considering fluid–structure interaction (FSI). Numerical simulation for a free-flying structural model in transonic speed is completed. Results show that the small elastic deformation of the structure can greatly affect the FSI. The FSI vibration tests are carried out in a transonic speed wind-tunnel for checking numerical theory and algorithms, and the wind-tunnel test results well accord with that of the numerical simulation. This indicates that the presented numerical method can be applied to predicting the structural dynamics responses when containing the FSI.

1. Introduction

A high-speed flying structure in the air will undergo complicated and unstable aerodynamic circumstances. The strong aerodynamic force acting on the flying structure can cause strong structural dynamic response. This harmful vibration can damage the electronic equipment fixed in the structure. Therefore, accurately predicting the dynamic response of structure interacting with high-speed airflow is an important topic. Souli and Zolesio[1] developed a computational procedure to solve the problems of viscous incompressible flows under large free surface motions. The arbitrary Lagrangian–Eulerian (ALE) method was used to move the free surface nodes as well as the internal nodes. The coupling of the mesh equations of motion and the fluid equations was essentially done through the free surface boundary conditions. An elastic model with free surface boundary conditions was used to model the mesh motion. The boundary condition at the free surface was deduced from the fact that no fluid particle can cross the free surface. Guruswamy[2] pointed out that the domain decomposition approaches required efficient interfaces

* Corresponding author. Tel.: +86 29 88431000.
E-mail addresses: yjyan_2895@nwpu.edu.cn (Y. Yan), shanzhizhang86@163.com (S. Zhang).

Peer review under responsibility of Editorial Committee of CJA.

Production and hosting by Elsevier

http://dx.doi.org/10.1016/j.cja.2014.12.027
1000-9361

techniques when fluids and structures were solved in independent computational domains for aerospace applications. Though fluid–structure interaction (FSI) techniques for solutions from equations based on low-fidelity approaches which were in the linear domain were well advanced and were incorporated in production codes NASTRAN and ASTROS, those computations involved high-fidelity equations such as the Navier–Stokes for fluids and finite elements for structures' interface approaches were still under development.

This paper also provides a technical overview of the methods about interfacing flow solutions from the Euler/Navier–Stokes methods with structural solutions using modal/finite-element methods. Aquelet et al.[3] used the ALE technique to solve fuel slosh problem and a new ALE formulation for the fluid mesh was developed to keep the fluid mesh integrity. Lohner et al.[4] developed a volume of fluid technique and coupled with an incompressible Euler/Navier–Stokes solver operating on adaptive, unstructured grids to simulate the interactions of extreme waves and three-dimensional structures. Extrapolation algorithms were used to obtain velocities and pressure in the gas region near the free surface. Results demonstrate that the presented approach could simulate violent free surface flows with strong nonlinear behavior. Dettmer and Peric[5] evaluated Newton type solution strategies for the strongly coupled system of equations arising in the computational modeling of FSI and pointed that the essential part of all ALE type solution strategies was the fluid mesh motion. They investigated the effect of the terms which coupled the fluid flow with the fluid mesh motion on the convergence behavior of the overall solution procedure and also indicated that the computational efficiency of the simulation of many FSI processes, including fluid flow through flexible pipes, could be increased significantly if some coupling terms were calculated exactly. Jo et al.[6] developed the finite element based on lattice Boltzmann method to model complex fluid domain shapes. Their study addressed a new finite element formulation of the lattice Boltzmann equation using a general weighted residual technique. Among the weighted residual formulations, the collocation method, Galerkin method and method of moments were used for finite element-based Lattice Boltzmann solutions. Guruswamy[7] presented a modular process for efficiently solving large-scale multidisciplinary problems using single-image cluster supercomputers. The process could integrate multiple disciplines with diverse physical characteristic while retaining the efficiency of individual disciplines. Computational domain independence of individual disciplines was maintained using a meta programming approach. The procedure included an efficient load balancing scheme suitable for parallel computers. Results were demonstrated for large-scale aerospace problems. Lohner et al.[8] also offered a convenient and cost-effective approach for coupling computational fluid dynamics and computational structural dynamics codes without rewriting them.

At present, the researches on the FSI of general fluid and structures are substantial and there are also many test studies.[9–15] However, the FSI studies and tests in a wind tunnel on aerodynamic or aircraft are not many, and the retrieved literatures are few.[16–18] Especially, the research model in this paper is a missile model, and its FSI and tests in wind tunnel are scarcely reported so far. Because computational fluid dynamics is more complex and difficult, the structure is often taken as rigid in aerodynamic calculation. The difficulty will be greater if one considers simultaneously the structural rigid body motion and elastic deformation vibration and this topics is still a research frontier and hotspot. The new idea of this paper mainly lies in two aspects, one is the structural rigid displacement and elastic deformation states are simultaneously transferred to Euler solver as a new boundary condition of fluid through coupling-interface, the other is to carry out the FSI test verification of a missile model in high-speed wind tunnel.

2. Numerical algorithms and scheme for FSI

The fluid analysis depends on Euler solver. Based on conservation of mass, momentum and energy of fluid, Euler equation of motion can be written as

$$\frac{\partial \boldsymbol{q}}{\partial t}+\frac{\partial f(\boldsymbol{q})}{\partial x}+\frac{\partial g(\boldsymbol{q})}{\partial y}+\frac{\partial h(\boldsymbol{q})}{\partial z}=0 \tag{1}$$

where $\boldsymbol{q}$ is the state vector; $f(\boldsymbol{q})$, $g(\boldsymbol{q})$ and $h(\boldsymbol{q})$ denote the fluxes of the conserved state variables. They are expressed as follows:

$$\begin{aligned} \boldsymbol{q}&=\begin{bmatrix}\rho\\ \rho u\\ \rho v\\ \rho w\\ E\end{bmatrix}, f(\boldsymbol{q})=\begin{bmatrix}\rho u\\ \rho u^2+p\\ \rho uv\\ \rho uw\\ (E+p)u\end{bmatrix},\\ g(\boldsymbol{q})&=\begin{bmatrix}\rho v\\ \rho uv\\ \rho v^2+p\\ \rho vw\\ (E+p)v\end{bmatrix}, h(\boldsymbol{q})=\begin{bmatrix}\rho w\\ \rho uw\\ \rho vw\\ \rho w^2+p\\ (E+p)w\end{bmatrix}\end{aligned} \tag{2}$$

where ρ is the material density, u, v, and w denote the velocity components, p is the pressure and E is the total energy. For the air, because five equations with six unknowns have been established, the system can be closed by adding the equation of state for ideal gas:

$$p=(\gamma-1)\rho e \tag{3}$$

where e represents the specific internal energy of the air, and γ the ratio of specific heats.

Generally, solving of Euler equation of motion Eq. (1) depends on numerical method, and the first step is to divide the space field into Euler meshes, the second step is to solve the Euler equation of motion for every element through finite volume method.

The flux of element surface can be figured by flux function:

$$f_{\mathrm{R}}\left(\boldsymbol{q}^{\mathrm{L}},\boldsymbol{q}^{\mathrm{R}}\right)=\frac{1}{2}\left[f(\boldsymbol{q}^{\mathrm{L}})+f(\boldsymbol{q}^{\mathrm{R}})\right]-\frac{1}{2}\left(\sum_{i=1}^{5}\tilde{\alpha}_i|\tilde{\lambda}_i|\tilde{\boldsymbol{R}}_i\right) \tag{4}$$

where $\tilde{\alpha}_i$ is the wave strength, $\tilde{\lambda}_i$ the eigenvalue and $\tilde{\boldsymbol{R}}_i$ the eigenvector. The superscript "L" denotes the left state variables, and the superscript and subscript "R" all denote the right state variables.

The calculation precision of element face flux can be governed by the way in which the left and the right element state variables are determined. If state variable values of the left and the left-left element are involved, the second order precision of computational scheme in space can be attained, and an interpolation algorithm is used to calculate the state flux of left side of an element face. The same method is used for the calculation of right-side face flux of an element.

For the left side of an element face, calculation scheme with second-order precision can be expressed as

$$\boldsymbol{q}_{i+1/2}^{\mathrm{L}} = \boldsymbol{q}_i + \Psi^{\mathrm{L}}(\boldsymbol{q}_i - \boldsymbol{q}_{i-1})/2 \tag{5}$$

where

$$\Psi^{\mathrm{L}} = \frac{1}{2}\left[(1-\kappa)\Phi(\boldsymbol{r}^{\mathrm{L}}) + (1+\kappa)\boldsymbol{r}^{\mathrm{L}}\Phi(1/\boldsymbol{r}^{\mathrm{L}})\right] \tag{6}$$

and

$$\boldsymbol{r}^{\mathrm{L}} = \frac{\boldsymbol{q}_{i+1} - \boldsymbol{q}_i}{\boldsymbol{q}_i - \boldsymbol{q}_{i-1}} \tag{7}$$

Calculation scheme for the right side is similar to it. The inverse algorithm is defined for $\kappa = -1$ and the penalty function Φ is defined as

$$\Phi(\gamma) = \max[0, \min(2\gamma, 1), \min(\gamma, 2)] \tag{8}$$

Coupled with the above computational scheme in space, a three-stage time integration scheme is developed as

$$\boldsymbol{q}^{(0)} = \boldsymbol{q}_i^n \tag{9}$$

$$\boldsymbol{q}^{(1)} - \boldsymbol{q}^{(0)} = -\frac{\alpha_1 \Delta t}{V_i}\boldsymbol{F}^{(0)} \tag{10}$$

$$\boldsymbol{q}^{(2)} - \boldsymbol{q}^{(0)} = -\frac{\alpha_2 \Delta t}{V_i}\boldsymbol{F}^{(1)} \tag{11}$$

$$\boldsymbol{q}^{(3)} - \boldsymbol{q}^{(0)} = -\frac{\alpha_3 \Delta t}{V_i}\boldsymbol{F}^{(2)} \tag{12}$$

$$\boldsymbol{q}_i^{n+1} = \boldsymbol{q}^{(3)} \tag{13}$$

$$\boldsymbol{F}^{(k)} = \sum_{n=1}^{6} f_{\mathrm{R}}(\boldsymbol{q}_{\mathrm{L}}^{(k)}, \boldsymbol{q}_{\mathrm{R}}^{(k)})A_n \tag{14}$$

where $\boldsymbol{q}^{(k)}$ expresses the state variable value for integration Step k, α_k the coefficient for Step k, and A_n the area of an element face.

Body-fitted meshes are often used for the calculation of flow field in FSI problem. But in the following numerical simulation, the displacement of structural model is too large and it will cause the body-fitted meshes severe deformation. Therefore, immobile meshes are employed. When the structure moves in the flow field, its surface intersects the meshes. Euler solver will figure out the data denoting the positions of intersection points and these data are used to determine the flow boundary.

The structural analysis depends on Lagrangian solver. This solver employs finite element method in space field and explicit time integration scheme in time field. Structural equation of motion is

$$\boldsymbol{M}\boldsymbol{a}_n + \boldsymbol{C}\boldsymbol{v}_n + \boldsymbol{K}\boldsymbol{d}_n = \boldsymbol{F}_n^{\mathrm{ext}} \tag{15}$$

where $\boldsymbol{a}_n$ denotes the acceleration vector, $\boldsymbol{v}_n$ the velocity vector, $\boldsymbol{d}_n$ the displacement vector, $\boldsymbol{M}$ the mass matrix, $\boldsymbol{C}$ the damping matrix, $\boldsymbol{K}$ the stiffness matrix, and $\boldsymbol{F}_n^{\mathrm{ext}}$ the vector of externally applied loads at Step n.

Equation of motion Eq. (15) can be rewritten as

$$\boldsymbol{a}_n = \boldsymbol{M}^{-1}(\boldsymbol{F}_n^{\mathrm{ext}} - \boldsymbol{C}\boldsymbol{v}_n - \boldsymbol{K}\boldsymbol{d}_n) \tag{16}$$

Applying central difference scheme, a recursive progress in time field can be written as

$$\boldsymbol{v}_{n+1/2} = \boldsymbol{v}_{n-1/2} + \boldsymbol{a}_n(\Delta t_{n+1/2} + \Delta t_{n-1/2})/2 \tag{17}$$

$$\boldsymbol{d}_{n+1} = \boldsymbol{d}_n + \boldsymbol{v}_{n+1/2}\Delta t_{n+1/2} \tag{18}$$

There exist two schemes to solve FSI problem. One is the loosely-coupled or domain-decomposition scheme, and the other is the tightly-coupled scheme. For the latter, the equation of motion for both fluid and structure are synchronously solved using a single computational domain. However, it is numerically inefficient or even impossible to solve fluid and structure using a monolithic numerical scheme. Therefore, the domain-decomposition scheme is adopted in the following numerical simulation. The overall procedure of this scheme is as follows:

(1) Assume that the state of fluid at time-step t_n is known and the state of structure will not change during the interval between t_n and t_{n+1}, then the solutions for fluid at time-step t_{n+1} can be calculated through Euler solver.
(2) Exert the aerodynamic force obtained from the above step on the structural model and then compute the solutions for structure at time-step t_{n+1} through Lagrangian solver.
(3) Transfer the structural rigid displacement and elastic deformation state to Euler solver as a new boundary condition of fluid through coupling-interface.
(4) Make $n = n + 1$ and repeat the above steps until the end time.

3. Numerical analysis for free-flying structural model

Because the airflow field surrounding aircraft in transonic flight stage is especially complicated, the vibration of aircraft structure at this stage is noteworthy. The presented numerical algorithm and scheme can be used to study the transonic dynamic characteristic of a free-flying structure. A shell structural model is shown in Fig. 1.

It is divided into 4-node shell elements. In Fig. 1, Point D denotes a studied point on the surface of structural frustum section in which the control apparatuses are usually installed. When the structure flies in air, it will undergo gravity and thrust. Suppose that the thrust is evenly distributed on the structural bottom surface and keeps acting during the whole simulative flight course. Direction of thrust paralleling to x-axis is just opposite to that of gravity. Supposing the initial flight direction is along x-axis and the initial velocity value of structure is 305 m/s, the structure will speed up from subsonic to supersonic flight if thrust value is bigger than gravity value. Euler region is modeled and divided into 8-node elements by rectangle immobile meshes. It is shown in Fig. 2 that a and b respectively denote the structural initial and ultimate positions in this simulation.

The structural material parameters used in numerical calculation include density, elastic modulus and Poisson's ratio, and the physical parameters of gas include primal density, adiabatic exponent and dynamic viscosity value.

At the beginning moment of computing, the structural dynamic response is probably unstable because of the abrupt action of thrust and aerodynamic force. Therefore, a uniform motion stage of structure is added. The whole simulative flight of structure is 0.7 s long. Suppose that V_x denotes x-compo-

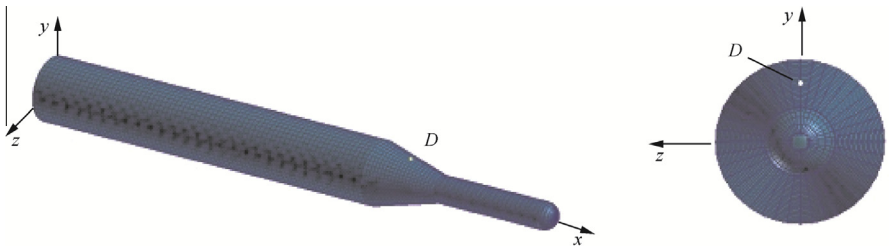

Fig. 1 Free-flying shell structural model in numerical simulation.

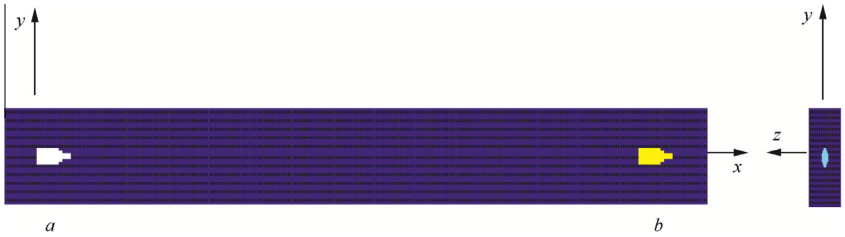

Fig. 2 Euler region in free-flying simulation.

nent of flight velocity. In this simulation, the value of thrust keeps 89 kPa with V_x approximately keeping 305 m/s during the initial 0.2 s and 235 kPa with V_x speeded up from 305 m/s to 360 m/s during the remaining 0.5 s.

In a usual method dealing with FSI problem, a rigid model is used to determine the aerodynamic force acting on it and then the force is exerted on the corresponding elastic model to compute its dynamic response. Because the effect of structural elastic deformation on aerodynamic force does not be calculated, the result obtained from this method is probably not accurate. In this numerical simulation, rigid and elastic models are employed, respectively, and the response results of them are compared.

V_x values of Point D in time domain for rigid and elastic models are shown in Fig. 3.

It can be seen that the V_x value in Fig. 3(b) can be obtained by adding a small fluctuation to V_x value in Fig. 3(a). Structural elastic deformation produces the fluctuation. For both rigid and elastic models, V_x value increases at the rate of about 160 m/s from 0.2 s to 0.5 s and at the rate of about 35 m/s from 0.5 s to 0.7 s. It indicates that the increase of flight velocity will become difficult in transonic flight. It is just an important characteristic of transonic flight. Because the thrust value keeps constant in transonic flight, it can be concluded that the value of aerodynamic drag must sharply augment at about $t = 0.5$ s when Mach number approaches 1.0. Suppose that a_x denotes x-component of acceleration. a_x values of Point D in time domain for rigid and elastic models are shown in Fig. 4.

In Fig. 4(a), a_x value sharply decreases at about $t = 0.5$ s, which just accords with the change regularity of V_x value shown in Fig. 3(a) for rigid model. However, this sharply change does not occur in Fig. 4(b). The a_x value keeps fluctuating in the vicinity of 0 m/s^2 for elastic model.

The power-density-spectrum (PSD) distributions of aerodynamic force of the rigid and elastic models and radial acceleration of the elastic model on Point D at the transonic flight stage are given in Fig. 5(a)–(c), respectively.

It can be found out that the great amplitude values of the force for the rigid model mainly congregate in a low and narrow frequency range (Fig. 5(a)). From Fig. 5(b) and (c), one

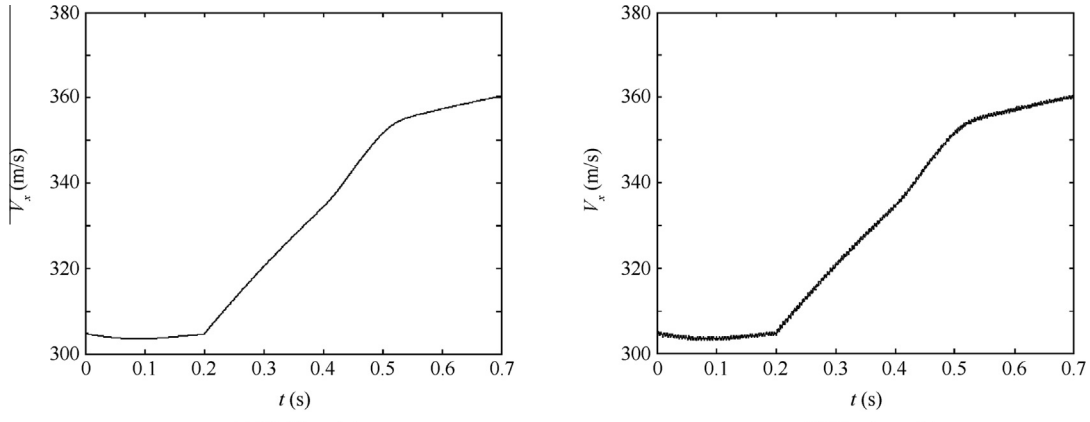

Fig. 3 Flight velocity of rigid and elastic models.

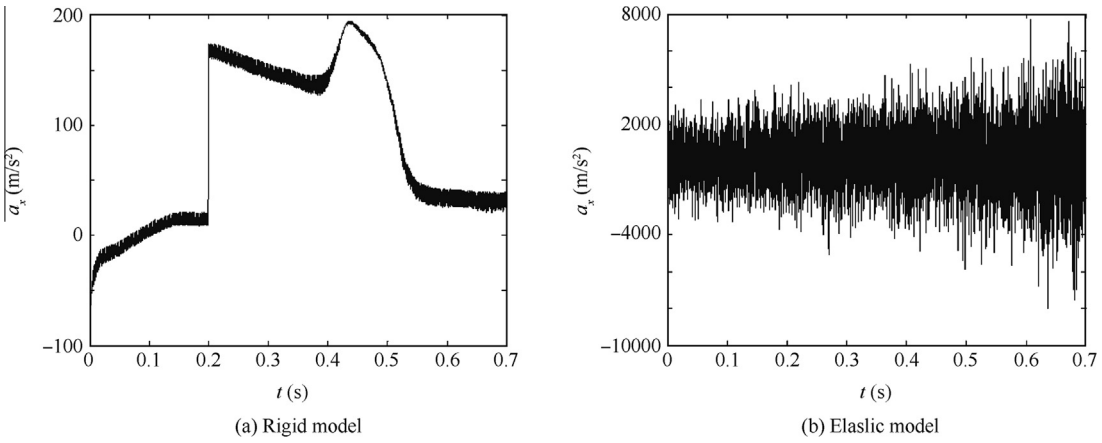

Fig. 4 Flight acceleration of rigid and elastic models.

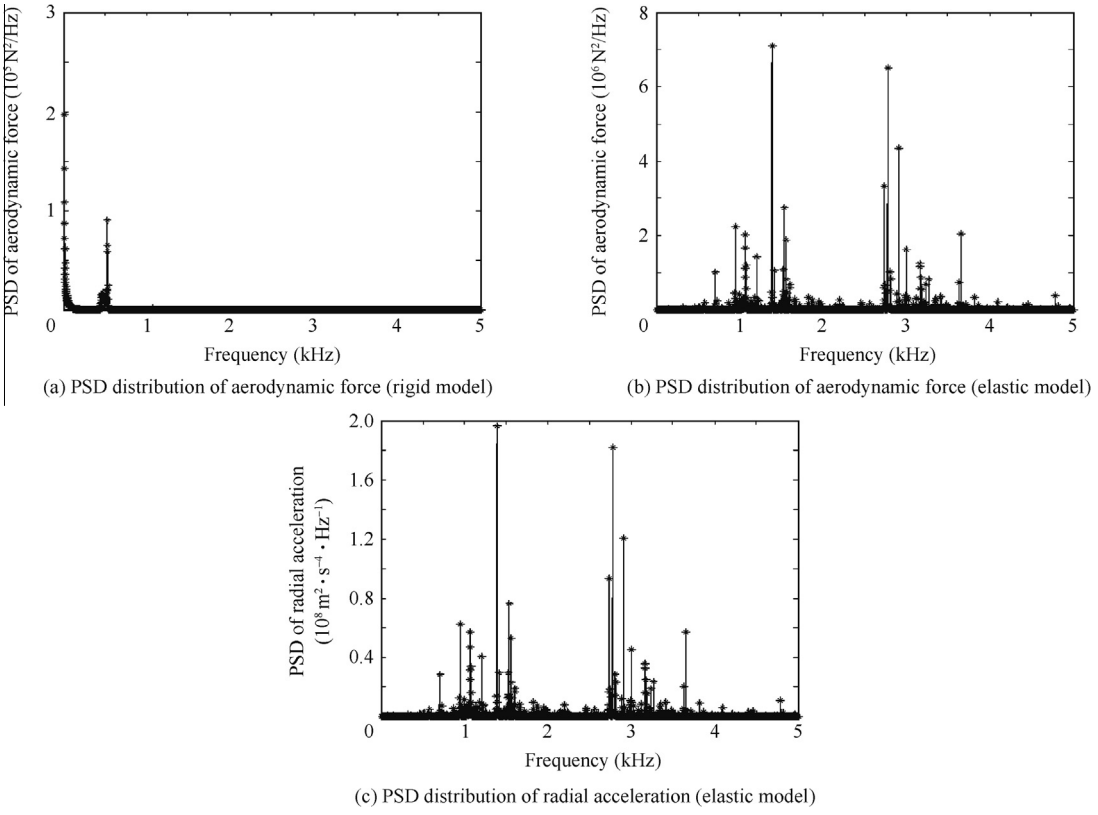

Fig. 5 PSD distributions of aerodynamic force and radial acceleration on Point *D*.

can also find that the PSD distribution of aerodynamic force is similar to that of vibration acceleration in frequency domain. This just proves that they are strongly correlative and the structural vibration belongs to the aerodynamic excited vibration. In Fig. 5(b) and (c), the distribution ranges of prominent amplitudes are from 700 Hz to 1700 Hz and 2600 Hz to 3700 Hz, and this is obviously different from the result of the rigid model. In fact, the elastic vibration of flying structure causes considerable disturbance to the surrounding airflow. And contrariwise, the disturbed airflow synchronously produces new structural elastic vibration. Therefore, structural elastic deformation plays an important role in FSI although elastic deformation is insignificant in contrast with rigid displacement in magnitude. It cannot be ignored in the calculation of aerodynamic force and structural dynamic response.

4. Wind-tunnel test and its numerical simulation

Test is the primary approach in research. Test result can be used to verify the numerical method. Firstly, a wind-tunnel test is carried out to study the dynamic characteristic of a thin-shell model in high-speed airflow. Secondly, this test is simulated through numerical method based on the presented numerical algorithm and scheme. Results of test and simulation are compared to show that the numerical method is feasible in qualitative analysis of structure.

4.1. Wind-tunnel test

An elastic thin-shell structural model used in transonic wind-tunnel test is designed and manufactured. Its size meets the test requirement that the blockage ratio is less than 0.01 and its thickness value is 0.5 mm. This model is shown in Fig. 6.

In order to decrease the interference of tail-support to test-section fluid field, this model is supported by a lengthened hollow pole and this pole is fixed out of the tunnel test-section. The fixing scheme of model is shown in Fig. 7. Thickness of tail-support is 1.0 cm. Therefore, it can be approximatively seen as a rigid body.

In this test, seven strain sensors are stuck on structural surface. Arrangement and serial numbers of sensors on measuring-points are shown in Fig. 8.

In Fig. 8, *B* denotes the structural apparatus-cabin section; *A* and *C* denote the sections next to *B*. Test equipment mainly includes continuous-pressurizing high-speed wind-tunnel, 8-channel strain amplifier and 32-channel data acquisition instrument. They are shown in Fig. 9.

The environment temperature is 17.4 °C, and the environment pressure is 97.30 kPa. Test Reynolds number is 15×10^6

Fig. 6 Elastic thin-shell structural model in transonic wind-tunnel test.

Fig. 7 Test model and tail-support in wind-tunnel.

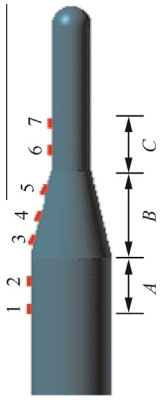

Fig. 8 Arrangement and serial number of strain sensors (side view).

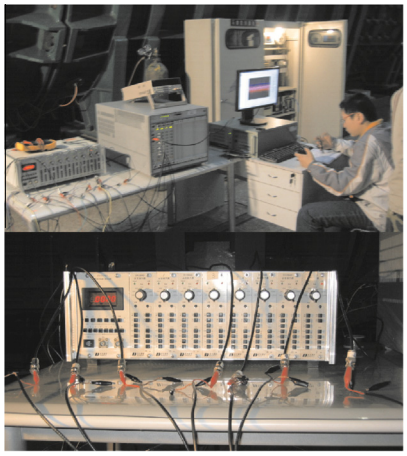

Fig. 9 Equipment in wind-tunnel test.

on condition that Mach number is 0.8, characteristic dimension of model is 0.225 m, and total air temperature is 318 K. Holes occur on the upper and lower walls of wind-tunnel to reduce the interference of walls to airflow field. Measurement of structural dynamic strain is carried out when Mach number respectively gets stable at 0.20, 0.30, 0.40, 0.50, 0.60, 0.70, 0.75, 0.80, 0.85, 0.90, 0.95, 1.00, and 1.05. The sampled signal from sensor is voltage signal $s(t)$. It can be transformed into strain signals ε through expression $\varepsilon = \beta s(t)$, in which β is a constant. It indicates that the voltage signal can be used in qualitative analysis of structural dynamic characteristic.

Firstly, PSD of signal is calculated. PSD distribution for measuring Point 3 (Point 4 is the closest to Point *D* in Fig. 1, but the data of Point 4 is not available) on condition that Mach number equals 0.85 is shown in Fig. 10.

It shows that the large signal amplitudes concentrate in about 2065 Hz in frequency domain and these amplitudes are much bigger than those corresponding to other frequencies. It indicates that the shell structure interacting with high-speed flow vibrates mainly at about 2065 Hz. The conclusions at other Mach numbers are the same.

Secondly, the vibration signal energies for these measuring points are calculated and they will be used to study the distri-

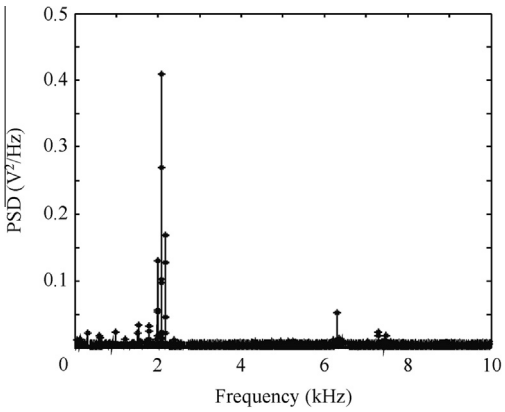

Fig. 10 Signal PSD distribution of measuring Point 3 for test model.

bution of vibration energy. The distribution of signal energy ratio Er_i for the case of Mach number equaling 0.85 is shown in Fig. 11.

$E_{ri} = E_i/E_{i=7}$, $E_i = s^2(t_j)$. The E_{ri} expresses the energy ratio for measuring Point i, E_i the signal energy of Point i, and $s(t_j)$ the signal value at sampling time t_j. Failure occurs to Point 4, so the data sampled from it will not be considered. Value of Point 4 has already been deleted in Fig. 11. It can be seen that the energy ratios of Points 6 and 7 which are located on Section C are bigger than those of other points. It shows that the elastic vibration of Section C is the most intense. The average of E_{r3} and E_{r5} is a little bigger than that of E_{r1} and E_{r2}. It indicates that the energy average of Section B is a little stronger than that of Section A.

Finally, vibration signal energies E_i at all Mach numbers are computed. The distributions of signal energy for Points 7 and Point 3 at 13 Mach numbers are shown in Fig. 12(a) and (b), respectively.

From Fig. 12(a), it can be found out that the energy value will sharply change when Mach number equals 0.90. Similar case also happens to Point 3. Rapid decrease occurs in the energy values of Points 1, 2, 3, and 5 when Mach number increases from 0.75 to 0.80. Sharp change of E_i is probably caused by the great variation of aerodynamic force when Mach number approaches 1.00.

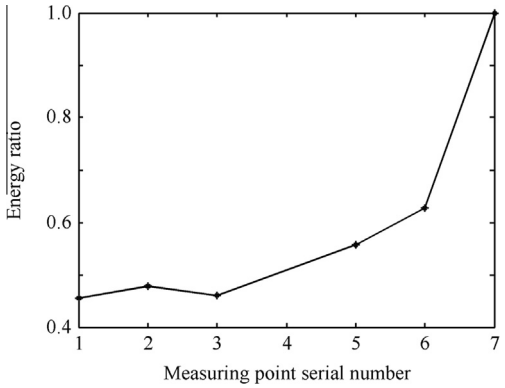

Fig. 11 Vibration energy distribution for test model.

4.2. Numerical simulation for wind-tunnel test

The structural model for numerical simulation according to the actual size of test model and tail-support is established. The surface of this numerical model acts as the coupling-interface on which the FSI takes place. Numerical model is divided into 4-node shell elements. The model with meshes is shown in Fig. 13.

In Fig. 13, the Section D expresses the thin-shell structure, and the Section E the tail-support. Nodes on the Section F are restricted to no displacement and rotation. Arrangement and serial numbers of measuring points and denotation of the Sections A, B, and C in numerical model are the same as those shown in Fig. 8.

Euler region surrounding the structural model is built to simulate the airflow field. It is divided into 8-node hexahedron elements with rectangular meshes and these meshes are immobile in calculation. If this region is too large, the time spent in simulative calculation will be excessively long. Considering this, the established Euler region only envelops partial tail-support. The Euler region and the meshes in it are shown in Fig. 14.

This region denotes a part of test-section of wind-tunnel, and the structural model in it is also shown in this figure. For this region, the boundary planes which cut z-axis express the perforated walls of wind-tunnel; those planes which cut y-axis denote the imperforate walls of wind-tunnel; others are free boundary planes. The direction in which the airflow enters this region is indicated in Fig. 14. Suppose that the Euler region is full of air at the initial time and the initial Mach number of airflow in this region is 0.85. The airflow Mach number at the entry plane keeps 0.85 in the whole simulation process.

Through numerical calculation based on the presented algorithm and scheme, result illuminating the vibration characteristic of structure is obtained. The fluctuation of V_z (radial velocity) in time domain for a point on Section B is given in Fig. 15, and it indicates that the numerical result will become stable after about 0.35 s.

Firstly, PSD distribution of strain for measuring Point 3 is shown in Fig. 16.

Compared with wind-tunnel test result given in Fig. 10, the predominant strain amplitudes of numerical model also concentrate in a narrow frequency range. These amplitudes appear at about 2635 Hz which are much higher than the low-order natural frequencies of structure. Therefore, it can be seen that the main dynamic response of structure interacting with high-speed airflow is not the usual low-order model response.

Secondly, vibration energies on seven measuring points in numerical model are also computed. The processing method of date is similar to that used for wind-tunnel test. Distribution of energy ratio E_{ri} for the case of Mach number equaling 0.85 is shown in Fig. 17.

Compared with Fig. 11, the energy ratios for Points 6 and 7 located on the Section C are also bigger than those of other points. And the average of E_{r3}, E_{r4} and E_{r5} also approaches to that of E_{r1} and E_{r2} .

4.3. Comparative analysis of test and numerical results

Vibration energy of the thin-shell structure mainly concentrates in a narrow high-frequency range in which the frequency

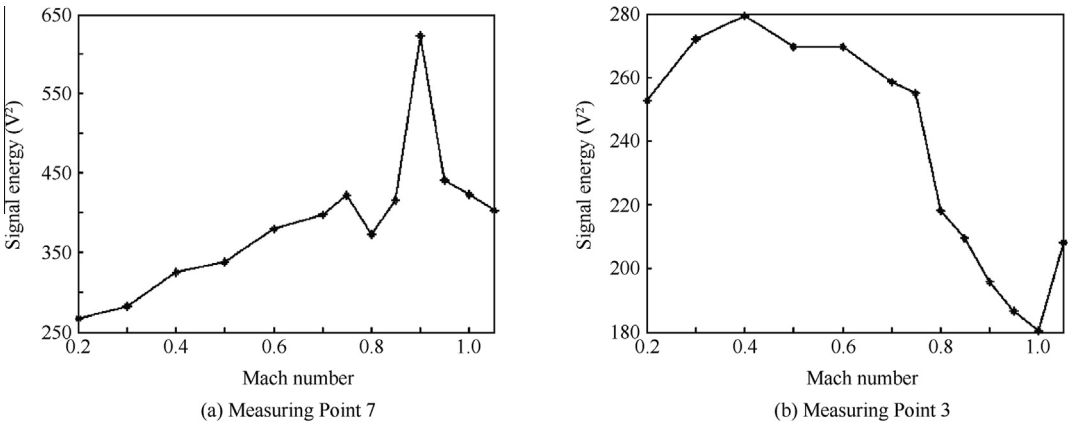

Fig. 12 Vibration energy of measuring Points 7 and 3.

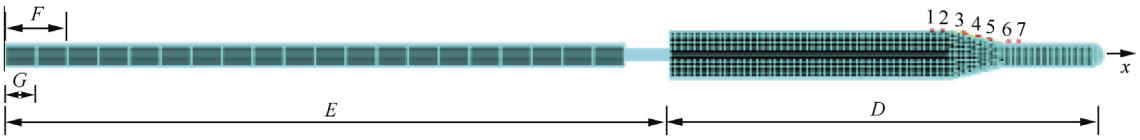

Fig. 13 Numerical model of thin-shell structure and tail-support.

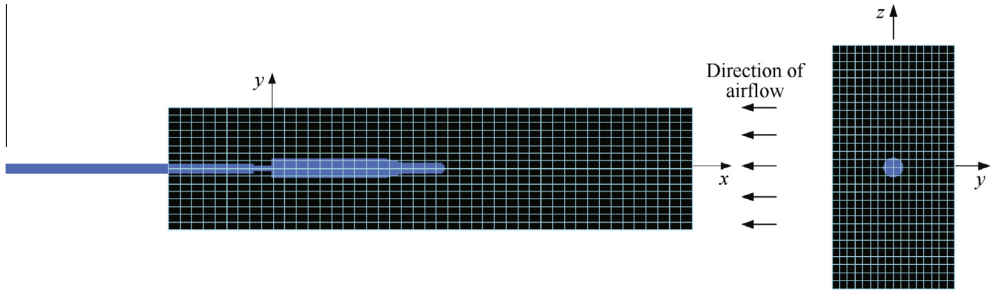

Fig. 14 Euler region and Euler meshes.

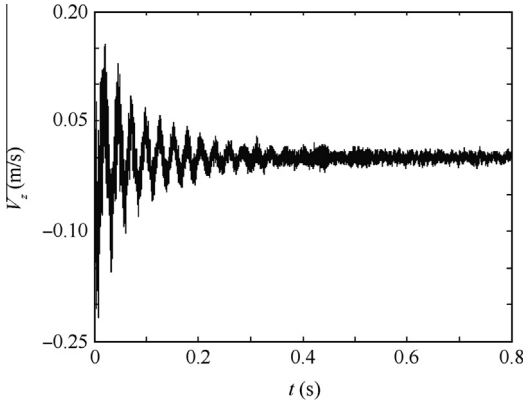

Fig. 15 Fluctuation of V_z in time domain.

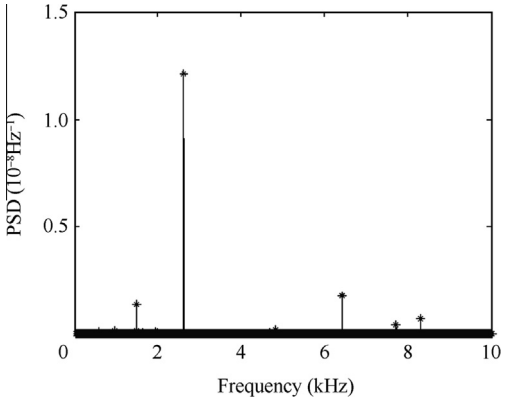

Fig. 16 Strain PSD distribution of measuring Point 3 for numerical model.

values are not the structural low-order natural frequencies. It indicates that the dominant dynamic response of structure is not the usual low-order model response. This structural dynamic characteristic can be obtained through the analysis of numerical result and it is proved by wind-tunnel test. It shows the numerical method based on the presented algorithm and scheme can be used in qualitative analysis of structural dynamics characteristic considering FSI. The main differences between numerical and test results are listed as follows:

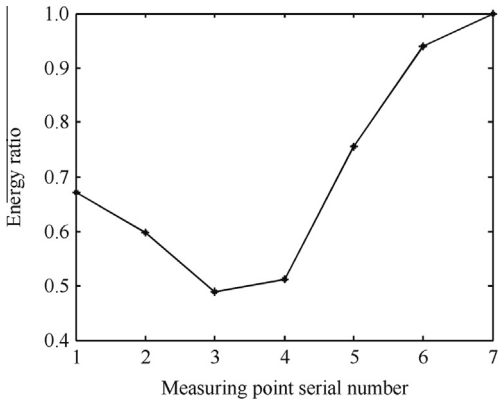

Fig. 17 Vibration energy distribution for numerical model.

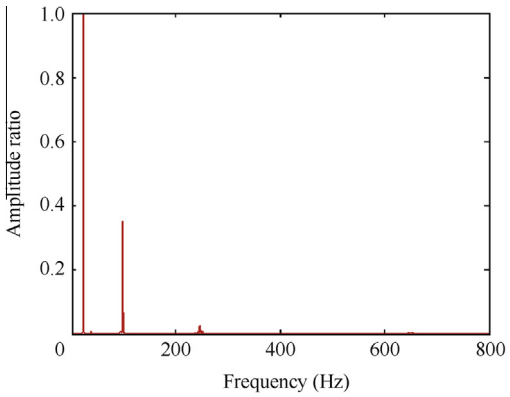

Fig. 18 Test result of natural frequency for test model.

(1) The largest amplitude of strain occurs at 2635 Hz for numerical model of structure but at 2065 Hz for tests one.
(2) Other obvious PSD amplitudes of strain distribute at 1500, 6420 and 7720 Hz for numerical model but at 1500, 6300 and 7300 Hz for test one.

These differences are considered to be caused by the distinction between numerical and test models. Lower-order natural frequencies of structural model are listed in Table 1.

Difference of natural frequency reveals that the dynamic characteristic of numerical model is not exactly the same as that of test one. It can be found out from Table 1 that natural frequency values of numerical model calculated with nodes on Section *F* restricted to no displacement and rotation are different from those in the case of Section *G* restricted. It indicates that the constraint of structure supposed in numerical simulation will affect the calculation result of structural dynamic response. In fact, the constraint of structure supposed in numerical simulation cannot be exactly the same as that of test structural model. In addition, the material parameters used in numerical calculation are probably not the same as those of test structural model. It can also lead to differences between numerical and test results. The testing result of natural frequency for test model is given in Fig. 18.

Test model contains the extended supporting rod at tail, which, together with the thin-shell structure, forms an elongated structure. Thus, the strong stiffness of tail supporting rod and great flexibility of the thin-shell will comprise a special structural system, and it is accurate to establish its dynamic model. Therefore, the measurement of natural frequencies is carried out to validate the established calculation model. In the test, hammer, acceleration sensor and LMS SCADAS III-TEST Lab are applied with the model clamped on its tail. The low-order natural frequencies of the calculated and test are listed in Table 1. Because the natural frequencies of the thin-shell are high and crowded, they cannot be measured using knocking method so that we cannot compare them to the calculated results. Therefore, the natural frequencies of thin-shell structure are not given out. Vibration modes of the first three orders of numerical model with Section *F* restricted are shown in Fig. 19.

Although Section *B* is the windward section, the vibration energy of measuring points on this section is not the maximum. The vibration of Section *C* is the most intense. The energy average of measuring points in Section *B* approaches to that in Section *A*. This dynamic characteristic of structure can be obtained from both numerical calculation and test.

In general, numerical method based on the presented algorithm and scheme can be applied to the qualitative analysis of structural dynamic response to high-speed airflow. However, the numerical result should be amended through abundant data

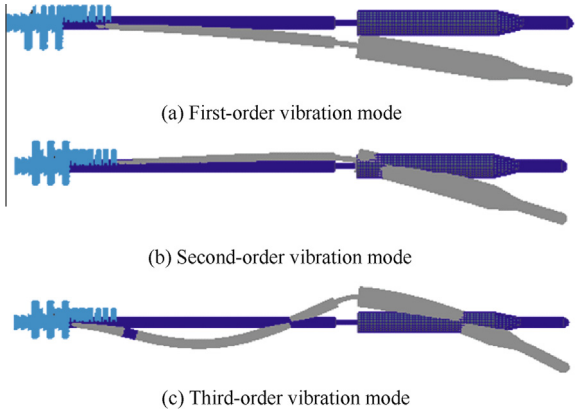

Fig. 19 Vibration modes of the first three orders of numerical model with Section *F* restricted.

Table 1 Low-order natural frequencies of structure.

Model	Natural frequency (Hz)					
	First-order	Second-order	Third-order	Fourth-order	Fifth-order	Sixth-order
Section *F* restricted	39.053	110.55	333.44	596.49	677.17	758.4
Section *G* restricted	36.134	106.87	305.24	596.49	663.04	718.9
Test model	23.44	98.44	246.09	602.93	618.36	647.66

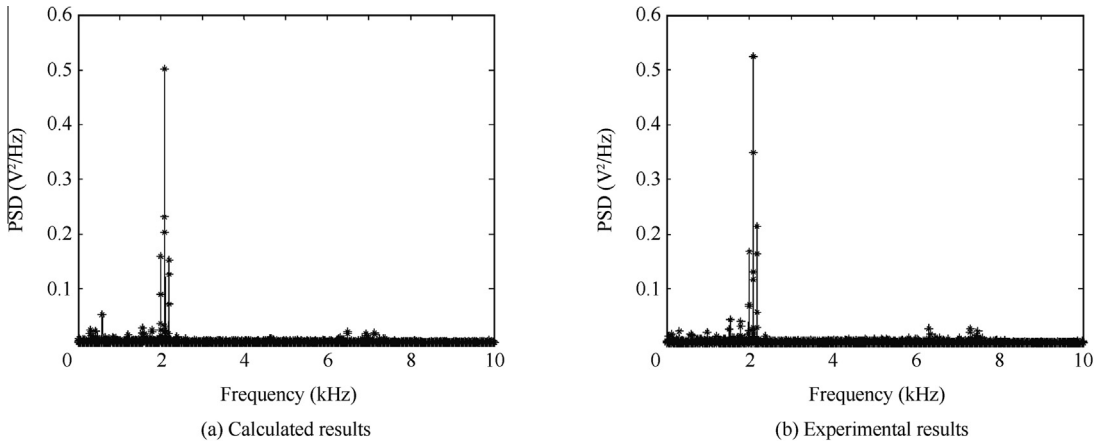

Fig. 20 Calculated and test dynamic strain response power spectrum.

from test in further. Obviously, the direct comparison between the calculated and test results of structural vibration responses under FSI is more convictive and also necessary. Therefore, the typical calculated and test results of the structural dynamic strain response power spectrum are shown in Fig. 20.

One can find that the results from two methods are basically consistent.

5. Conclusions

Results of numerical simulation for free-flying structural model indicate the following conclusions:

(1) The characteristics of aerodynamic force for rigid structural model and elastic one are extremely different in frequency domain. Structural elastic deformation cannot be ignored in dynamic analysis.
(2) The flight acceleration of aircraft will sharply reduce with the thrust keeping invariable in transonic flight.

Farther conclusions listed as follows are acquired through the results of wind-tunnel test and its numerical simulation:

(1) The present numerical algorithm and scheme can be used in qualitative analysis of structural dynamic response coupled with aerodynamic force.
(2) The predominant components of structural strain amplitudes concentrate in a narrow frequency range which does not contain the low-order natural frequencies of structure. The dynamic response of structure coupled with aerodynamic force is not the usual low-order model response.
(3) The elastic vibration energy of Section *B* (apparatus-cabin section) is not the strongest although it is the windward section.

In addition, test result shows that the structural elastic vibration energy will sharply changes when Mach number of airflow approaches 1.00.

Acknowledgements

This study was supported by the National Natural Science Foundation of China (No. 50875212) and Specialized Research Fund (priority development area) for the Doctoral Program of Higher Education of China (No. 20126102130004).

References

1. Souli M, Zolesio JP. Arbitrary Lagrangian–Eulerian and free surface methods in fluid mechanics. *Comp Methods Appl Mech Eng* 2001;**191**(3):451–66.
2. Guruswamy GP. A review of numerical fluids/structures interfaces methods for computations using high-fidelity equations. *Comp Struct* 2002;**80**(1):31–41.
3. Aquelet N, Souli M, Gabrys J, Olovson L. A new ALE formulation for sloshing analysis. *Struct Eng Mech* 2003;**16**(4):423–40.
4. Lohner R, Yang C, Onate E. Simulation of flows with violent free surface motion and moving objects using unstructured grids. *Int J Numer Methods Fluids* 2007;**53**(8):1315–38.
5. Dettmer WG, Peric D. On the coupling between fluid flow and mesh motion in the modeling of fluid–structure interaction. *Comp Mech* 2008;**43**(1):81–90.
6. Jo JC, Roh KW, Kwon YW. Finite element based formulation of the Lattice Boltzmann equation. *Nucl Eng Technol* 2009;**41**(5):649–54.
7. Guruswamy GP. Development and applications of a large scale fluids/structures simulation process on clusters. *Comp Fluids* 2007;**36**(3):530–9.
8. Lohner R, Cebral J, Yang C, Baum JD, Mestreau E, Charman C, et al. Large-scale fluid–structure interaction simulations. *Comp Sci Eng* 2004;**6**(3):27–37.
9. Kannan R, Harrand V, Tan XG, Yang HQ, Przekwas AJ. Highly scalable computational algorithms on emerging parallel machine multicore architectures II: development and implementation in the CSD and FSI contexts. *J Parallel Distr Comp* 2014;**74**(9):2808–17.
10. Annerel S, Claessens T, Degroote J, Segers P, Vierendeels J. Validation of a numerical FSI simulation of an aortic BMHV by in vitro PIV experiments. *Med Eng Phys* 2014;**36**(8):1014–23.
11. Nayer GD, Kalmbach A, Breuer M, Sicklinger S, Wuechner R. Flow past a cylinder with a flexible splitter plate: a complementary experimental-numerical investigation and a new FSI test case (FSI-PfS-1a). *Comp Fluids* 2014;**99**(1):18–43.
12. Teich M, Gebbeken N. Analysis of FSI effects of blast loaded flexible structures. *Eng Struct* 2013;**55**(1):73–9.
13. Swillens A, Taelman L, Degroote J, Vierendeels J, Segers P. Comparison of non-invasive methods for measurement of local pulse wave velocity using FSI—simulations and in Vivo data. *Ann Biomed Eng* 2013;**41**(7):1567–78.

14. Borna A, Habashi WG, McClure G, Nadarajah SK. CFD-FSI simulation of vortex-induced vibrations of a circular cylinder with low mass-damping. *Wind Struct* 2013;**16**(5):411–31.
15. Duvernois V, Marsden AL, Shadden SC. Lagrangian analysis of hemodynamics data from FSI simulation. *Int J Numer Methods Biomed Eng* 2013;**29**(4):445–61.
16. Takizawa K, Tezduyar TE, Kostov N. Sequentially-coupled space-time FSI analysis of bio-inspired flapping-wing aerodynamics of an MAV. *Comp Mech* 2014;**54**(2):213–33.
17. Wick T. Flapping and contact FSI computations with the fluid-solid interface-tracking/interface-capturing technique and mesh adaptivity. *Comp Mech* 2014;**53**(1):29–43.
18. Korobenko A, Hsu MC, Akkerman I. Structural mechanics modeling and FSI simulation of wind turbines. *Math Models Methods Appl Sci* 2013;**23**(2):10–50.

Yan Yunju received his Ph.D. degree from Institute of Vibration Engineering, Northwestern Polytechnical University in 1998. Currently he is working in School of Mechanics, Civil and Architectures Northwestern Polytechnical University as a Professor. His research interests include aircraft vibration and noise analysis, aeroengine fault diagnosis, and structural damage vibration detection.

Xi Zhuyou received M. S. from Xi'an University of Architecture and Technology in 2005. Currently he is an associate professor at Liaoning University of Technology, Jinzhou, China. His research interests include structural damage diagnosis theory and application, structural health monitoring and signal processing.

Zhang Shanzhi received his Ph.D. degree from Institute of Vibration Engineering, Northwestern Polytechnical University in 2011. Currently he is working in China Eastern Airlines as a senior engineer. His research interests include aircraft vibration and noise analysis, aeroengine fault diagnosis.